

A Statistical Study of De-Embedding Applied to Eye Diagram Analysis

Paul D. Hale, *Senior Member, IEEE*, Jeffrey Jargon, *Senior Member, IEEE*, C. M. Jack Wang, Brett Grossman, Mathew Claudius, José L. Torres, Andrew Dienstfrey, and Dylan F. Williams, *Fellow, IEEE*

Abstract—We describe a stable method for calibrating digital waveforms and eye diagrams by use of the measurement system response function and its regularized inverse. The function describing the system response includes the response of the oscilloscope and any associated cables and test fixtures. We demonstrate the effectiveness of the method by performing a statistical analysis of the calculated eye height and eye width obtained from a controlled experiment consisting of multiple cable lengths, bit rates, and oscilloscope samplers. We also demonstrate our approach by measuring the transmission through a test device consisting of a short length of cable, a ball-grid array socket, and a complicated circuit board.

Index Terms—Deconvolution, de-embedding, eye diagram, eye pattern, inverse problems, regularization.

I. INTRODUCTION

IN the radio and microwave frequency regime, components are often fabricated on-wafer or are surface-mounted onto printed circuit boards to reduce manufacturing costs and power consumption, while increasing signal bandwidth and yield. Measurements of these components invariably include probing pads, vias, and interconnects to coaxial interfaces. In this case, de-embedding techniques are required to remove the parasitics from the raw measurements to extract the intrinsic device properties. At high frequencies, techniques that make use of frequency-domain scattering-parameter matrices are typically employed, for example [1] and [2].

By contrast, embedded components for digital applications are often characterized in the time domain. A common configuration uses a sampling oscilloscope to measure a bit sequence, supplied by a pattern generator or on-board processor, and

transmitted through a passive interconnect and/or test fixture. The results of such a measurement are displayed in the form of a sampled waveform or eye diagram [3]. As in the microwave problem, de-embedding requires the removal of impedance mismatches of the source and receiver (pattern generator and oscilloscope), and insertion loss and mismatch of cables and/or test fixtures. Additionally, data acquired on an oscilloscope require corrections for the impulse response and timing errors of the oscilloscope.

Mathematically, the de-embedding problem in both the microwave and the digital scenarios is the same; frequency domain division of the measured signal by the system response function. However, the nature of the system response function for the time-domain measurement is of a fundamentally different character. This is because the bandwidths and dynamic ranges required for high fidelity digital signal measurements can be orders of magnitude larger than for typical microwave measurements. Simultaneously, the response function for all oscilloscopes asymptotically exhibit a low-pass filter characteristic. Therefore, recovery of the time-domain signal with good fidelity requires large amplification at some frequencies. Naively de-embedding fixture loss and the response of the oscilloscope by use of the simple division procedure can result in unacceptable amplification of measurement noise. Instead, regularized deconvolution, which balances accuracy with noise amplification, must be employed. In contrast to frequency-domain de-embedding, only recently has there been an industry-wide effort to investigate the accuracy of de-embedding techniques for digital applications, for example, see [4].

In this paper, we propose a technique for de-embedding that uses regularized deconvolution and is appropriate for measurements made with equivalent-time sampling oscilloscope. We quantitatively show how correction for timebase errors and de-embedding through the use of regularized deconvolution can yield stable signal reconstructions with increased eye height and eye width margins. We validate the numerical algorithms by varying the bit rate, cable length, and the type of oscilloscope sampler to quantify the reproducibility of the technique. Our analysis provides two conclusions: 1) Signal impairments arising from measurement configurations including cabling and sampling oscilloscope can result in significant differences in eye-diagram measurements, and 2) regularized de-embedding with a stable parameter selector is capable of consistently correcting for some of these impairments. We quantify both claims by analysis of variance. Finally, we demonstrate the use of the algorithms for a problem of practical interest, i.e.,

Manuscript received January 4, 2011; revised June 3, 2011; accepted July 16, 2011. Date of publication September 26, 2011; date of current version January 5, 2012. This work is a contribution of the National Institute of Standards and Technology and is not subject to copyright in the U.S. The Associate Editor coordinating the review process for this paper was Dr. Rik Pintelon.

P. D. Hale and J. Jargon are with the Optoelectronics Division, National Institute of Standards and Technology (NIST), Boulder, CO 80305 USA (e-mail: hale@boulder.nist.gov).

C. M. J. Wang is with the Statistical Engineering Division, National Institute of Standards and Technology, Boulder, CO 80305 USA.

B. Grossman is with the Intel Corporation, Hillsboro, OR 97124 USA.

M. Claudius is with the Intel Corporation, Santa Clara, CA 95054 USA.

J. L. Torres is with the Intel Corporation, Chandler, AZ 85226 USA.

A. Dienstfrey is with the Applied and Computational Mathematics Division, National Institute of Standards and Technology, Boulder, CO 80305 USA.

D. F. Williams is with the Electromagnetics Division, National Institute of Standards and Technology, Boulder, CO 80305 USA.

Color versions of one or more of the figures in this paper are available online at <http://ieeexplore.ieee.org>.

Digital Object Identifier 10.1109/TIM.2011.2164853

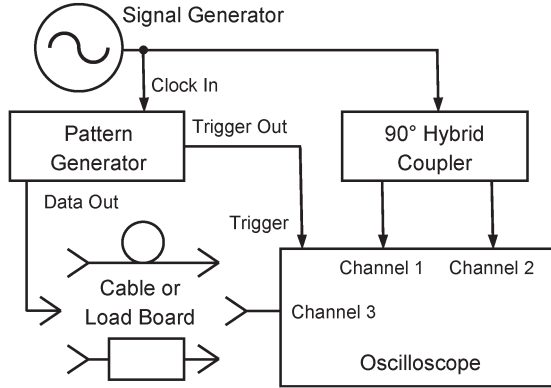


Fig. 1. Schematic diagram of the measurement apparatus. The synthesized signal generator produces sine waves that are used to correct for jitter and timebase distortion in the sampling oscilloscope.

characterization of the degradation of signals transmitted through a ball-grid array socket and printed-circuit board.

II. DECONVOLUTION

In this section, we show how mismatch, loss, and instrument response can be de-embedded by regularized deconvolution. We consider an apparatus for generating a digital pattern and transmitting the signal directly, or through a length of cable, to a sampling oscilloscope, as is shown in Fig. 1.

When the oscilloscope is connected directly to the signal generator, the signal measurement is distorted by impedance mismatch and the finite response time of the sampler. When the generator is connected to the oscilloscope through a lossy cable or adapter, the signal measurement is further distorted by frequency-dependent loss. Given the oscilloscope measurement $v_s(t)$,¹ we wish to solve for $v_g(t)$, the voltage the generator would deliver to a 50Ω load, uncorrupted by the effects of the measurement system.

Following the exposition of [5], we model the ideal measurement as a linear time-invariant system with noise. Therefore, the measured voltage v_s can be written as a convolution of the system impulse response function $h(t)$ with v_g . That is

$$v_s(t) = \int_0^{\infty} h(\tau)v_g(t - \tau)d\tau + n(t) \quad (1)$$

where h is the impulse response function including, where appropriate, contributions from loss and impedance mismatch. See Appendix A (11), (17), and (20) for example. The problem of solving for v_g in (1) is the well-studied inverse problem of deconvolution. Theoretical and practical aspects of solving inverse problems are described in, for example, [6]–[9].

In practice, the oscilloscope samples the voltage at discrete times $t_n = t_0 + n\Delta t$ to obtain the measured waveform vector $\mathbf{v}_s = (v_s(t_0), \dots, v_s(t_{N-1}))^T$. We can then replace the continuous convolution in (1) above with a discrete approximation. We furthermore treat the convolution as if it were periodic.

¹We denote the continuous time-domain functions by lower-case italics, e.g., v and h , the discretized representation of a function or measurement in bold face, i.e., \mathbf{v} , matrix operators as bold-face upper case, i.e., \mathbf{H} , and their discrete Fourier transforms (DFTs) with hats as $\hat{\mathbf{v}}$ and $\hat{\mathbf{H}}$.

Potentially, this is a nontrivial assumption, as described in [16]. After ensuring that the conditions for a periodic approximation are met, we replace the integral equation of (1) by a matrix equation

$$\mathbf{v}_s = \mathbf{H}\mathbf{v}_g + \sigma\mathbf{n} \quad (2)$$

where the matrix \mathbf{H} is circulant, the waveform vector \mathbf{v}_g is periodic with period T , and the additive noise is assumed to be uncorrelated and is represented as the product of a random normal vector \mathbf{n} , with unity standard deviation and the noise standard deviation σ .

As \mathbf{H} is circulant, it is diagonalized by the DFT. In the frequency domain, the system (2) is equivalent to

$$\hat{\mathbf{v}}_s = \hat{\mathbf{H}}\hat{\mathbf{v}}_g + \sigma\hat{\mathbf{n}} \quad (3)$$

where $\hat{\mathbf{H}} = \text{diag}(\hat{h}_1, \dots, \hat{h}_N)$ is the diagonal matrix of discrete Fourier coefficients of the sampled response function, and $\hat{\mathbf{n}}$ is the image of the noise vector \mathbf{n} under the DFT. For our impulse response functions, all entries $|\hat{h}_n| \neq 0$, thus, $\hat{\mathbf{H}}$ is invertible by division by the Fourier coefficients; $\hat{\mathbf{H}}^{-1} = \text{diag}(\hat{h}_1^{-1}, \dots, \hat{h}_N^{-1})$. More generally, one may always define the least-squares solution to (3). However, while it is a theorem that the least-squares inversion of (3) provides the minimum variance unbiased estimator of $\hat{\mathbf{v}}_g$, it is also well known that this estimator is often unacceptable, as the operator \mathbf{H} is ill-conditioned ($|\hat{h}_j|$ is small for some j) causing noise amplification to dominate the inversion. This behavior is common in inverse problems, and the usual solution is to introduce some form of regularization into the inversion.

In this paper, we regularize by use of the Tikhonov regularized inverse ([6]–[9]) along with truncation of the Fourier expansion at 110 GHz (a limitation of our calibration method, see Section III-A). Here, we summarize the Tikhonov method. Given a penalty operator \mathbf{L} and a scalar value λ , the least-squares normal equations are replaced by a regularized counterpart:

$$\hat{\mathbf{v}}_g(\lambda) = (\hat{\mathbf{H}}^*\hat{\mathbf{H}} + \lambda^2\hat{\mathbf{L}}^*\hat{\mathbf{L}})^{-1}\hat{\mathbf{H}}^*\hat{\mathbf{v}}_s \quad (4)$$

where $\hat{\mathbf{H}}^*$ is the complex conjugate transpose of $\hat{\mathbf{H}}$.

There are several ways of deriving (4) that highlight different interpretations, see [7]. One derivation is based on the minimization of the functional $\|\mathbf{H}\mathbf{v}_g - \mathbf{v}_s\|^2$ subject to the constraint that the solution \mathbf{v}_g is picked from the subspace for which $\|\mathbf{L}\mathbf{v}_g\|^2$ is bounded. This leads to the minimization

$$\min_{\{\mathbf{v}_g \in \mathbb{R}^n\}} \{ \|\mathbf{H}\mathbf{v}_g - \mathbf{v}_s\|^2 + \lambda^2\|\mathbf{L}\mathbf{v}_g\|^2 \}. \quad (5)$$

In (4), prior information on the desired solution may be encoded by the choice of \mathbf{L} . For our problems, we expect that \mathbf{v}_g is twice differentiable and use the roughness penalty, $\mathbf{L} = \mathbf{D}_2$, where \mathbf{D}_2 is the periodized second-difference operator. Alternatively one may use $\mathbf{L} = \mathbf{I}$ corresponding to the less stringent constraint that the solution has bounded norm. We have found that the \mathbf{D}_2 choice gives better convergence for the problems we encounter in the context of waveform metrology [5].

For a given system response operator \mathbf{H} and penalty function \mathbf{L} , the Tikhonov equation (4) contains a free regularization

parameter λ . Under one interpretation, λ provides a mechanism for balancing the variance/bias trade off. For $\lambda = 0$, one observes that $\hat{\mathbf{v}}_g(0)$ is the least-squares solution, which is unbiased but exhibits a high variance, i.e., the noise is often unacceptably large. For large λ , the penalty term dominates the denominator of (4), smoothing the estimate of \mathbf{v}_g . In the limit $\lambda \rightarrow \infty$, $\mathbf{v}_g(\lambda) \rightarrow \mathbf{0}$ resulting in an estimator that is 100% biased but exhibits zero variance.

For a regularization framework to be rigorous and reproducible, it must state clearly the method by which one chooses the value of λ . We call such methods *selectors*. The inverse problems community has produced a diverse literature on various selectors but with little quantitative comparison until very recently (see [8], [10], and [11]). The question of which selector is best is very context specific. Early work in regularized deconvolution applied to waveform metrology used subjective methods for determining the regularization parameter, as in [12] and [13]. Later work, such as [14], advocated a more systematic approach. Absent detailed analysis of the selector, in the appropriate context, the practitioner is left questioning the regularization parameter choice, severely limiting the value of de-embedding when applied to eye-pattern measurements.

Recently, [5] provided a preliminary quantitative analysis demonstrating that the *L-curve* selector performs favorably in the context of waveform metrology. The L-curve, so named because of its resemblance to the letter “L,” is the graph of $(\|\mathbf{H}\mathbf{v}_g(\lambda) - \mathbf{v}_s\|, \|\mathbf{L}\mathbf{v}_g(\lambda)\|)$ plotted on a log-log scale. These norms are readily measurable and act as diagnostics of the behavior of the inversion with respect to λ . By varying λ , either norm can be minimized at the expense of the other. The L-curve selector is heuristic, the idea being that the value of λ that “best” balances the roughness (noise) against the residual (bias) is the $\lambda = \lambda_*$ corresponding to the corner of the L-curve. The usual definition of the corner, used here, is the point of maximum convex curvature, although other definitions are described in the literature, for example, see [15, pp. 110–111]. Detailed descriptions and examples of the L-curve method are given in [6], [8], and [16].

Because there are several other λ selectors whose performance is yet to be quantified in the context of waveform metrology problems, the best choice of selector is an issue of continuing investigation. The performance of our selector and our regularized deconvolution will be discussed in the context at hand in Sections III-C and IV.

III. SIGNAL TRANSMITTED THROUGH LOSSY CABLES

We first investigate our ability to calibrate measurements of a random bit sequence transmitted through a length of cable and measured with a sampling oscilloscope. The calibration removes the effects of cable loss, impedance mismatch, and sampler response to obtain an estimate of the time-domain waveform the generator would deliver to an ideal 50Ω load. We quantify the effectiveness of our waveform calibration by use of a statistical analysis of the eye diagrams associated with measurements made with varying cable lengths (losses) and with samplers that have different response functions and reflection coefficients.

A. Measurement Configuration and Calibration

The apparatus of Fig. 1 and our measurement procedures are designed to correct for timebase errors and the measurement system response. Although various techniques are available, we use the National Institute of Standards and Technology (NIST) timebase correction technique [17] to correct for jitter and timebase distortion. The synthesized signal generator produces a sine wave that is used as a clock for the pattern generator. This signal is also fed into a 90-degree hybrid coupler that produces quadrature sinusoids that are measured on channels 1 and 2 of the sampling oscilloscope. The output of the pattern generator is connected to the sampler in channel 3, either directly or through cables, and is measured simultaneously with the sinusoids on channels 1 and 2.

Because all of the samplers in the oscilloscope are activated by the same trigger pulse and timebase, the timing errors in all of the channels in the oscilloscope mainframe are nearly identical. The NIST timebase correction software [18] uses an orthogonal distance regression technique [19] to fit the sinusoids and estimate the timing error in their measurement. We then use this estimate to compensate for the timing error (timebase distortion and jitter) in each sample of the signal of interest (from the pattern generator).

To maximize the bandwidth of the calibrations, we dedicate 1.0 mm adapters to each of the oscilloscope samplers, cables, and pattern generator, which originally had either 2.4 mm or 1.85 mm connectors. This provides a single-mode interface up to 110 GHz. The response of the measurement system, including the response of the oscilloscope samplers, impedance mismatch, and cable loss, is calibrated up to 110 GHz by use of the formulas derived in Appendix A. To fully calibrate our measurements, it is necessary to consider such high frequency (greater than 17 harmonics of our highest data rate of 12.8 Gbit/s divided by two) because signal energy in our averaged measurements is clearly visible above the noise level at frequencies as high as 90 GHz to 100 GHz. However, the system response above 110 GHz could not be calibrated, and consequently $\hat{\mathbf{v}}_g$ was set to zero above 110 GHz as in [16]. This is an acceptable approximation because the signal is smaller than the noise at frequencies above 110 GHz in all cases studied here.

The impulse response of each sampler was calibrated [20] by use of a photodiode that had been characterized with NIST’s electro-optic sampling system in 200 MHz increments to 110 GHz [21]–[25], and the absolute scaling was determined by a swept sine technique [26]. The response and reflection coefficient of the oscilloscope were approximated on a 12.5 MHz frequency grid by linear interpolation of the 200 MHz data, which is a reasonable approximation because of the smooth response of the samplers and the short electrical length of the transmission lines from which they are constructed. The scattering parameters of the cables were measured in 12.5 MHz increments up to 67 GHz [27]. The loss of the cables at frequencies above 67 GHz was extrapolated from the lower-frequency measurements by fitting S_{21} to a model of the form (from [28]) $S_{21} = \exp(-Cf^{1/2} - iDf)$, where C and D are real constants. The reflection coefficients of the cables were assumed to be zero above 67 GHz. The

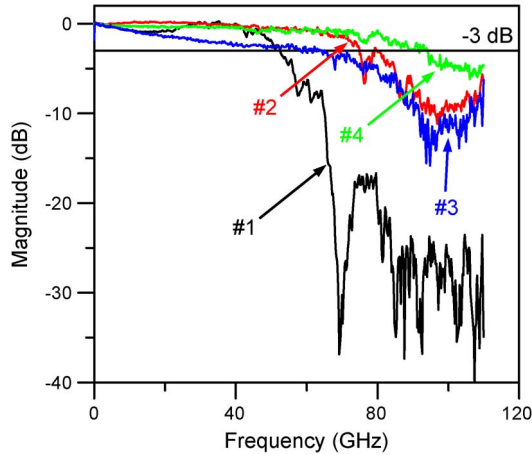


Fig. 2. Response of samplers used in this study. Samplers #1–#3 are the same as used in [16]. Sampler #4 is a newer model with about 90 GHz bandwidth.

approximations above 67 GHz are acceptable because the fraction of the energy in the random bit sequence above 67 GHz is very small (10^{-5}). Deviations of the actual performance of the components away from these simplifying assumptions would have only second-order effects. Nonrepeatable variations, such as those due to high-order modes, may appear as variations between repeat measurements. Finally, to check for potentially time varying source impedance, we measured the reflection coefficient of the generator when set to the high and low states and found essentially the same result for both settings.

All measurements were made with the pattern generator programmed to produce a 256-bit random sequence that contained 128 zeros and 128 ones with amplitude 0.5 V.

B. Data Acquisition

We measured the signal both directly and transmitted through three coaxial cables of varying lengths at three bit rates (3.2 Gbit/s, 6.4 Gbit/s, and 12.8 Gbit/s) by use of four different samplers. The magnitude of the sampler response functions is shown in Fig. 2. The three coaxial cables were designed for mode-free transmission up to at least 50 GHz and had lengths of 0.6096 m (24 in.), 1.524 m (60 in.), and 3.048 m (120 in.). The loss of the cables at 50 GHz was 4.01 dB, 7.23 dB, and 13.07 dB, respectively.

The signal for each cable/bit rate/sampler combination was initially sampled at $N = 65,536 = 2^{16}$ points in an 80.4-ns epoch by concatenating together eight groups of 8192 points, each spanning nominally consecutive 10.05 ns epochs [17]. This gave us an average sample interval of 1.2 ps, while the fastest 10% to 90% transition duration in our measurements was approximately 12 ps.

After correction for timebase errors, the corrected epoch duration (for our oscilloscope) was compressed slightly and the time interval between samples was nonuniform. To facilitate further signal processing, we linearly interpolated the corrected waveform to N evenly spaced points in an 80.0 ns epoch that was entirely inside the initially measured waveform. This 80.0 ns epoch corresponded to an integral number of periods of our 256 bit pattern at each of the bit rates we considered. For each cable/bit rate/sampler combination, we acquired a data set

consisting of 100 waveforms and, after interpolation, averaged them to obtain the voltage waveform vector \mathbf{v}_s . We found that the drift in the measurements was small and so we did not align the 100 waveforms before averaging. The above measurement procedure was repeated on three different dates. In total, we measured 144 averaged waveform vectors \mathbf{v}_s corresponding to 3 dates, 4 samplers, 4 cable lengths, and 3 bit rates.

C. Results

Eye diagrams are a particularly convenient way to visualize and quantify various features of long digital waveforms. We constructed eye diagrams from each of the 80.0 ns waveform vectors by use of the technique outlined in Appendix B. Fig. 3 shows eye diagrams that are constructed after various processing steps, demonstrating their effects. The plots give time in terms of unit intervals on the x -axis and voltage on the y -axis. Eye diagrams constructed from the averaged waveforms measured with the 12.8 Gbit/s direct signal, sampler #1, without and with correction for timebase errors are shown in Fig. 3(a) and (b), respectively. The timebase error increases approximately linearly with increasing epoch duration, causing the near closure of the eye diagram constructed from our waveform with 80.0 ns duration. Clearly, timebase errors must be addressed when long waveforms are used.²

Next, the effects of sampler response, mismatch, and cable loss are de-embedded by deconvolution of the appropriate system response function as given by (11) or (17). For the waveforms acquired with sampler #1 or with the other samplers and the longer cables, regularization was necessary. For example, Fig. 3(c) and (d) show the eye diagram after least squares and regularized deconvolution of the same waveform used to construct Fig. 3(b). However, we found that the curvature of L-curves sometimes had multiple local maxima. In this case, we chose the λ_* corresponding to the rightmost L-curve corner, as suggested by [29]. The effect of adding the 120 in cable to the above measurement system and removal of its response is shown in Fig. 3(e) and (f).

The eye diagram constructed from the waveform for direct connection to the higher bandwidth sampler #2 is shown with only timebase correction in Fig. 3(g) and after deconvolution in Fig. 3(h). We observe that Fig. 3(d), (f), and (h) are visually similar to each other, but different from the diagrams that have not been corrected for the system response in Fig. 3(b) and (e), and even with the high bandwidth sampler in the post-transition regions as shown in Fig. 3(g).

In the cases of the higher bandwidth samplers (#2–#4), the curvature of the L-curve had only a weak maximum and, moving to the left, a region of flat curvature, followed by possibly multiple values of very high curvature at the lowest values of λ . We speculate that the weak maximum and constant curvature region may be due to the regularizing effect of the hard cutoff at 110 GHz in the calibrated system response function. The very large curvatures may be due to round-off error. Whatever

²We note that timebase correction options are available commercially and may give comparable or better performance to our acquisition and timebase correction procedure.

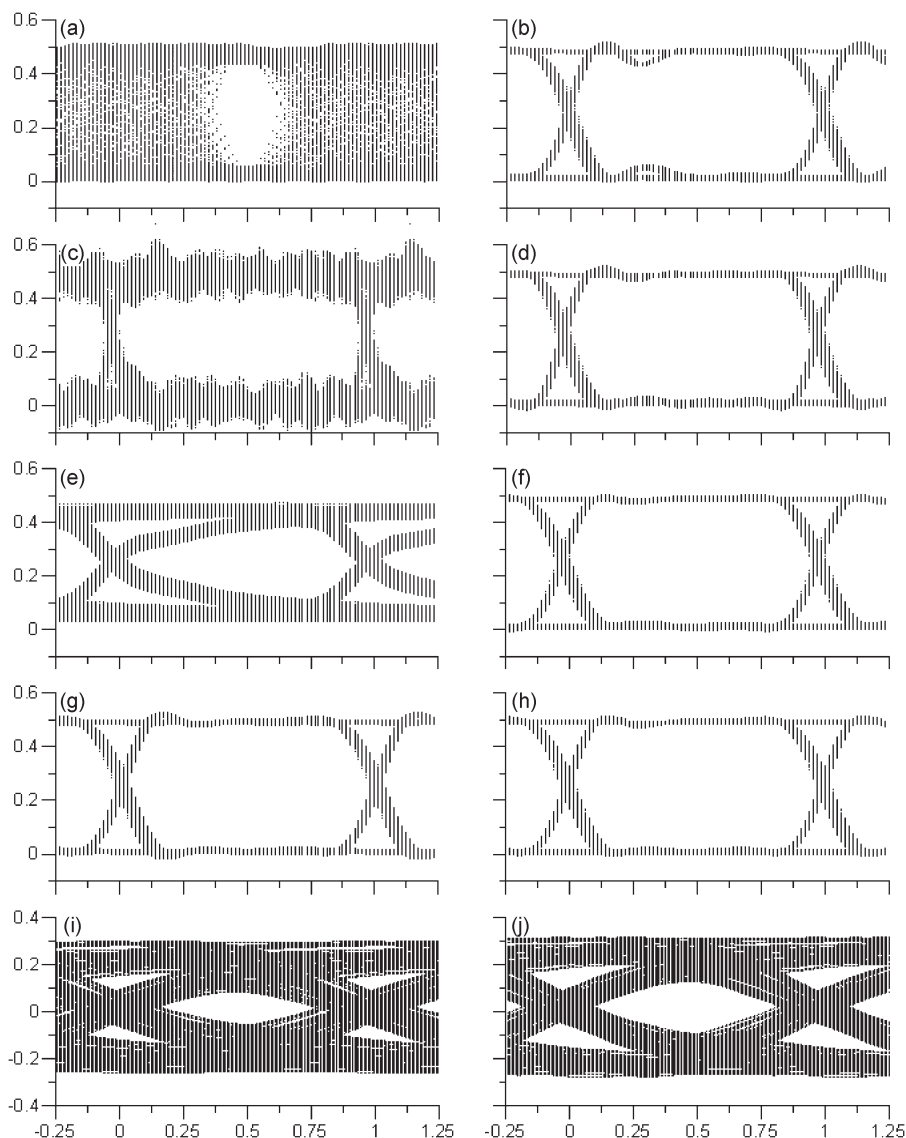


Fig. 3. Plots show voltage on y -axis and time in terms of unit intervals on the x -axis. Eye diagrams at 12.8 Gbit/s were constructed from the (a) waveform as measured with direct connection to sampler #1, (b) waveform shown in (a) corrected for timebase errors, (c) waveform shown in (b) with correction/deconvolution of system response but without regularization, (d) waveform shown in (b) with regularized deconvolution. Eye diagrams constructed from timebase corrected waveform for transmission through the 120 in cable (e) without deconvolution and (f) with regularized deconvolution. Eye patterns constructed from timebase corrected waveform for direct connection to sampler #2 (g) with only correction for timebase errors and (h) with regularized deconvolution. Timebase corrected eye diagrams constructed from a typical 6.4 Gbit/s 256 bit signal transmitted through the the 60 in cable and the printed circuit board (discussed in Section IV) are shown in (i) without correction for the system response and (j) with regularized deconvolution.

the cause of these features, it is clear that implementation of a robust selector requires further study. A fruitful line of investigation might be found in [11], where it was suggested that the search space for λ be bounded. However, we ultimately found in these cases that there was little difference between choosing the λ corresponding to the weak maximum and setting $\lambda = 0$.

We next describe a detailed statistical analysis of the results to determine if the calibration has a significant and consistent effect on the measurements. We note that the calibration corrects for the response of the samplers and the mismatch and loss of the different cables. Although the bit rate changes the contribution from these effects before calibration, lingering dependence on bit rate after calibration may be explained by the intrinsic properties of the pattern generator or calibration applied.

1) *Normalized Eye Height*: We calculate the eye height from the central 20% of the eye diagram by use of the methods described in [30]. We define the *normalized eye height* as the measured eye height divided by the eye amplitude programmed into the pattern generator. We use analysis of variance (ANOVA, see [31]) to investigate the effects of sampler, cable length, and data rate on normalized eye height based on measurements with and without calibration. We partition the *total sum of squares* of deviation from the mean for un-calibrated eye height data into individual sums of squares corresponding to the main effects, two-factor interactions, three-factor interaction, and measurement error. These sums of squares and other results are summarized in the ANOVA table given in Table I. We use $A \times B$ to designate the interaction between factors A and B.

TABLE I
ANOVA TABLE FOR UN-CALIBRATED NORMALIZED EYE HEIGHT

	DF	Mean Sq	F-value	p-value
sampler	3	0.00443	101.13	0.000
cable	3	0.98926	22580.63	0.000
rate	2	0.11599	2647.55	0.000
sampler × cable	9	0.00029	6.54	0.000
sampler × rate	6	0.00074	16.79	0.000
cable × rate	6	0.02593	591.86	0.000
sampler × cable × rate	18	0.00008	1.88	0.027
measurement error	96	0.00004		

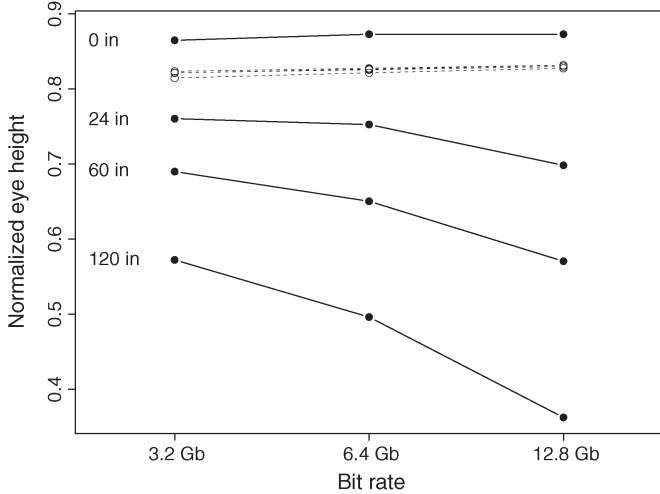


Fig. 4. Interaction plot for cable length and bit rate.

The first, second, and third columns contain, respectively, the name, the degrees of freedom, and mean sum of squares of each effect, which is obtained by dividing the sum of squares by its degrees of freedom. The F -value is the ratio of the effect's mean square to the mean square of measurement error. The last column contains the p -value for each effect, which is the probability of obtaining an F -value at least as extreme as the one that was actually observed, given that the *null* hypothesis is true [31]. The null hypothesis for sampler (the first row), for example, is that sampler has no effect on eye height. The smaller the p -value, the less likely the null hypothesis is true, or more significant the effect is. A commonly used threshold for p -value is 0.05. That is, we reject the null hypothesis and conclude that the effect is significant if its p -value is less than 0.05. Table I indicates that for normalized eye height all the main effects, two-factor, and three-factor interactions are significant.

A two-factor interaction, say, between cable length and bit rate can be explained by use of Fig. 4, which plots eye height versus bit rate at four different cable lengths for the un-calibrated data. The calibrated data are also shown (empty circles) and are shifted down by 0.05 to improve the presentation. It is obvious from the plot that the effect of bit rate in un-calibrated eye height is greater with 120-in cable than for the direct connection (0-in cable). The interaction arises from the differences in eye height due to change in bit rate for the four cable lengths. These differences are significant relative to measurement error. Because the main effect of a factor can be individually interpreted only if there is no evidence that the fac-

TABLE II
ANOVA TABLE FOR CALIBRATED NORMALIZED EYE HEIGHT

	DF	Mean Sq	F-value	p-value
sampler	3	0.0001019	5.50	0.002
cable	3	0.0002831	15.27	0.000
rate	2	0.0011506	62.07	0.000
sampler × cable	9	0.0000257	1.38	0.206
sampler × rate	6	0.0000332	1.79	0.109
cable × rate	6	0.0000155	0.84	0.545
sampler × cable × rate	18	0.0000032	0.17	1.000
measurement error	96	0.0000185		

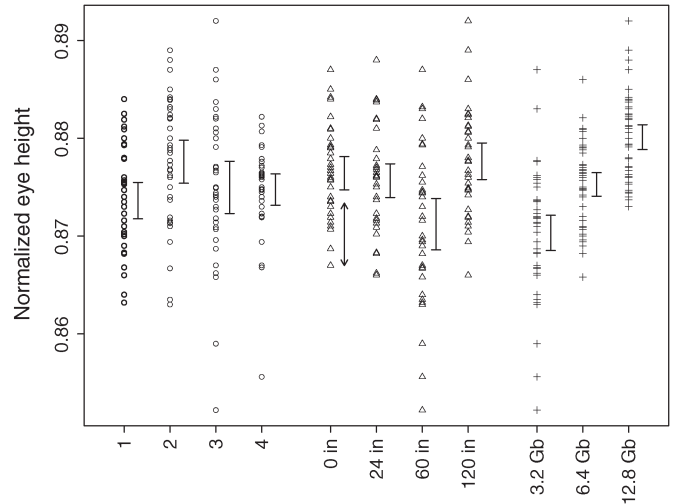


Fig. 5. Plot of calibrated normalized eye height as a function of four samplers (1 to 4), four cable lengths (0, 24, 60, 120 inches), and three bit rates (3.2, 6.4, 12.8 Gb). Error bars with flat heads indicate 95% confidence intervals of the corrected data. Error bar with arrow heads is 95% confidence interval of uncorrected measurement with no cable. Since the two error bars (with no cable) do not overlap, the correction is significant even when the oscilloscope is connected directly to the pattern generator.

tor interacts with other factors [31], we can draw no conclusion on how different samplers, cable lengths, and bit rates affect eye height by use of the un-calibrated measurements.

We next consider Table II, the ANOVA table based on calibrated eye height. Since Table II shows no evidence of interaction effects, we assume them to be zero and use a model containing only the main effects to analyze the data.

Fig. 5 plots calibrated eye height versus sampler, cable length, and bit rate. A 95% confidence interval for mean eye height for each sampler, cable length, and bit rate is also shown at the right side of the data. The confidence interval is based on the variance calculated from the data within each individual level.

Fig. 5 shows that the confidence intervals corresponding to the four samplers overlap with each other, indicating that after calibration, the sampler has no effect on eye height. The graphical analysis of Fig. 5 is equivalent to the result obtained from three separate one-way ANOVA on sampler, cable length, and bit rate. The one-way ANOVA on sampler, for example, produces a p -value of 0.05543 for sampler effect. This marginally insignificant p -value is seen by the two barely overlapping 95% confidence intervals of samplers 1 and 2.

The confidence interval corresponding to the 60-in cable length does not overlap with the intervals of the other three

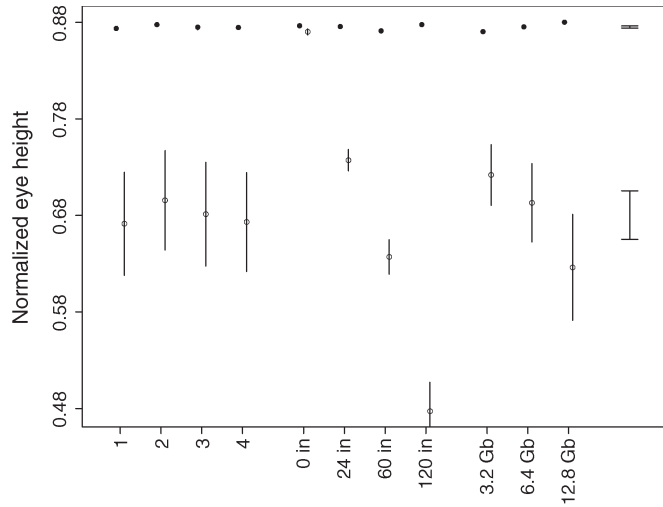


Fig. 6. Plot of difference between mean normalized eye height with calibration (solid circles) and mean normalized eye height without calibration (empty circles). Error bars are 95% confidence intervals of each factor while the rightmost column shows 95% confidence intervals pooled over all factors. Error bars for the calibrated data are too small to be visible on this scale but are shown in Fig. 5.

cable lengths. Consequently, cable length is a significant effect on eye height. However, if the seven smallest points from the 60-in column, which all have bit rate of 3.2 Gb, were removed from consideration, then the effect of cable length would not be significant at a 0.05 level. Fig. 5 also indicates that bit rate has a significant effect on eye height.

We offer two possible explanations for the significant effect of the bit rate on the eye height after calibration (right three columns of Fig. 5). 1) Since the (normalized) eye height is a function of the pattern generator calibration and software, it is possible that the eye height that the generator produces is actually a function of the bit rate because of a calibration error in the generator. For example, if the oscilloscope used for calibrating the generator's amplitude at the factory showed decreasing response for higher data rates, a calibration factor would have been applied that erroneously compensates by amplifying the signal more for high data rates. 2) Eye height measurements are based on the central 20% of the eye. As the bit rate decreases, the low-frequency content of the eye pattern increases. Low-frequency errors in the NIST oscilloscope calibration might cause a systematic error in the measured eye height that is bit-rate dependent. The low-frequency response of the oscilloscope could be better estimated by use of a swept-sine technique, as in [26]. Further investigation is required to determine the true explanation for this observed trend.

Next, we investigate whether calibration produces a significant change on eye height. Fig. 6 plots the mean eye height with calibration (solid circles) and without calibration (empty circles) for each level of sampler, cable length, and bit rate. It is apparent that the differences are substantial, both in magnitude and in variation (notice the scale in y -axis compared with the scale of the calibrated data shown in Fig. 5). Even in the case where no cable is included between the generator and the oscilloscope, the increase in eye height is significant (see Fig. 5) The rightmost column of Fig. 6 displays the 95% confidence intervals for mean eye height based on calibrated

TABLE III
ANOVA TABLE FOR UN-CALIBRATED NORMALIZED EYE WIDTH

	DF	Mean Sq	F -value	p -value
sampler	3	0.000087	5.07	0.003
cable	3	0.005504	320.23	0.000
rate	2	0.062431	3632.60	0.000
sampler \times cable	9	0.000037	2.16	0.031
sampler \times rate	6	0.000096	5.61	0.000
cable \times rate	6	0.003079	179.16	0.000
sampler \times cable \times rate	18	0.000014	0.81	0.677
measurement error	96	0.000017		

TABLE IV
ANOVA TABLE FOR CALIBRATED NORMALIZED EYE WIDTH

	DF	Mean Sq	F -value	p -value
sampler	3	0.0000773	3.59	0.017
cable	3	0.0000267	1.24	0.300
rate	2	0.0240668	1117.65	0.000
sampler \times cable	9	0.0000093	0.43	0.916
sampler \times rate	6	0.0000448	2.08	0.062
cable \times rate	6	0.0000133	0.62	0.715
sampler \times cable \times rate	18	0.0000213	0.99	0.478
measurement error	96	0.0000215		

and un-calibrated data. The separation of the two intervals indicates that the eye height is significantly increased due to calibration and the width of the confidence interval shows that the calibrated eye height is more stable than the un-calibrated eye height. From Figs. 5 and 6, we conclude that we have effectively and consistently removed the impairments on the measurement that are produced by cable loss and sampler response.

2) *Normalized Eye Width*: Next, we carry out the same analysis for normalized eye width, which we define as the eye width divided by the nominal bit period. We calculate the eye width by use of samples whose voltages are within $\pm 2\%$ of the crossing level (relative to the eye height) [30]. The analysis-of-variance table based on the un-calibrated data is given in Table III. Again, because the sampler, cable, and data rate interact with each other, we make no statement about the effects of each factor.

The analysis-of-variance table based on calibrated normalized eye width is given in Table IV. Since there is no evidence of interaction effects, we again examine each factor separately. Based on Figs. 7 and 8, we draw the following conclusions:

- 1) After calibration, sampler and cable length have no effect on normalized eye width.
- 2) The calibration increases the normalized eye width. The increase, averaging over different samplers, cable lengths, and bit rates, is significant.

Because the dependence on sampler and cable length has been removed, the remaining significant dependence on bit rate (shown clearly in the right three columns of Fig. 7) may be attributable to the intrinsic properties of the pattern generator. Because the normalized eye width is given by $(T - 6\sigma_j)/T$, where T is the bit period and σ_j is the jitter standard deviation, the decreasing trend in the last three columns of Fig. 7 might be explained by a roughly fixed generator jitter contribution (between 0.8 ps and 1.0 ps), while the the bit period decreases by a factor of four.

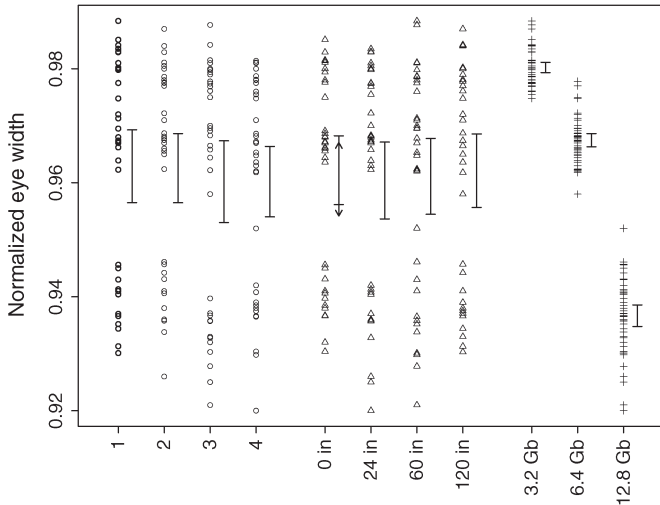


Fig. 7. Plot of calibrated normalized eye width as a function of four samplers (1 to 4), four cable lengths (0, 24, 60, 120 inches), and three bit rates (3.2, 6.4, 12.8 Gb). Error bars with flat heads indicate 95% confidence intervals of the corrected data. Error bar with arrow heads is 95% confidence interval of uncorrected measurement with no cable. Since the two error bars (with no cable) do overlap, the correction does not have a significant effect on normalized eye width when the oscilloscope is connected directly to the pattern generator.

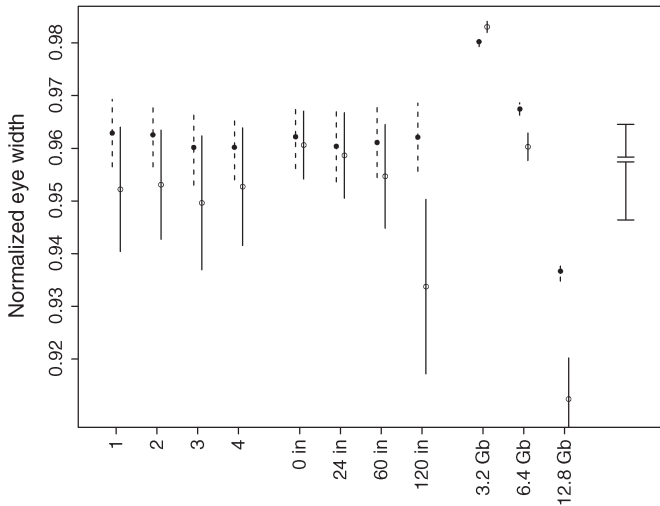


Fig. 8. Plot of difference between mean normalized eye width with calibration (solid circles, dashed error bars) and mean normalized eye width without calibration (empty circles, solid error bars). Error bars are 95% confidence intervals of each factor while the rightmost column shows 95% confidence intervals pooled over all factors.

IV. SIGNAL TRANSMITTED THROUGH A PRINTED CIRCUIT BOARD

Our second experiment was to characterize the transmission of a digital pattern through a complicated test structure that included short cables, a ball-grid array socket, and three different lanes (traces) of a printed circuit board. The goal of this experiment is to see if calibration removes the effects of sampler response, mismatch, and cable loss from the measured transmission of a device of practical interest. To be clear, we characterize transmission through the printed circuit board lanes and do not remove/de-embed distortions due to their presence. Thus, the measurand is the signal v_g convolved with the loss of the structure under test, as discussed in Appendix A.

We conducted transmission measurements of three lanes which were roughly 6 to 12 inches in length, at two bit rates (3.2 Gbit/s and 6.4 Gbit/s), three word lengths (32 bits, 128 bits, and 256 bits), two different cable lengths, and three different samplers. Because of time limitations, we measured only 24 of the possible 108 combinations. For these experiments, the pattern generator produced random sequences with amplitude 0.7 V. Data were acquired, corrected for timebase errors, interpolated to an 80.0 ns epoch, and averaged as before. The measurement was then calibrated (de-embedded, deconvolved) by use of the system response function given in (20) or (23) of Appendix A and the regularization techniques of Section II.

Example eye diagrams for a 6.4 Gbit/s measurement with the 60 in cable and printed circuit board are shown in Fig. 3(i) with timebase correction only, and in Fig. 3(j) after regularized deconvolution of the system response. Notice that although the eye opening is much smaller than in Fig. 3(d), (f), and (h), the effect of calibration is still quite noticeable.

We next proceed to a statistical analysis of the effect of calibration on the measurement of eye height and width. Note that we wish to test for significant changes in the eye height or eye width due to calibration. However, we expect that transmission through the PCB lanes with different reflections and frequency dependent loss will strongly depend on bit rate and word length so the factors lane, bit rate, and word length may remain significant after calibration.

A. Normalized Eye Height

The analysis-of-variance table for calibrated eye height and width is given in Table V. Because there are no repeated measurements, the F -statistic-based significance tests cannot be performed. For eye height data, we assume that all the interaction effects are negligible, which is a reasonable assumption given that the mean squares (column 3) corresponding to the interaction effects are relatively smaller than the mean squares of the main effects, so we can examine the effect of each factor individually. Based on the rightmost column of Fig. 9, showing 95% confidence intervals based on all 24 measurements, the calibration increases the eye height and the increase is significant. Also, bit rate appears to have significant effect on eye height, presumably due to the intrinsic properties of the lossy lanes. However, due to the small number of measurements, the error bars in some factors may not be too meaningful and a more extensive study, preferably with repeated measurements, is needed to make further conclusions regarding individual factors.

B. Normalized Eye Width

We assume that all the interaction effects for eye width are negligible, which is based on the fact that the mean squares (column 4 of Table V) corresponding to the interaction effects are relatively smaller than the mean squares of the main effects. From Fig. 10, we conclude that the calibration increases the eye width. However, the increase, averaging over different samplers, cable lengths, bit rates, lanes, and word lengths, is not significant. Again, the error bars in some factors may not be

TABLE V
ANOVA TABLE FOR TRANSMISSION THROUGH PRINTED CIRCUIT BOARD: CALIBRATED NORMALIZED EYE HEIGHT AND NORMALIZED EYE WIDTH

	DF	Height	Width
		Mean Sq	Mean Sq
sampler	2	0.000777	0.002444
cable	1	0.008767	0.010590
rate	1	0.096382	0.224446
lane	2	0.022908	0.013211
length	2	0.001936	0.001239
sampler \times cable	2	0.000362	0.000107
sampler \times rate	2	0.000065	0.001378
sampler \times lane	4	0.000535	0.000429
sampler \times length	3	0.000074	0.000193
cable \times rate	1	0.000259	0.000130
cable \times lane	2	0.000203	0.001005
rate \times length	1	0.000841	0.000961

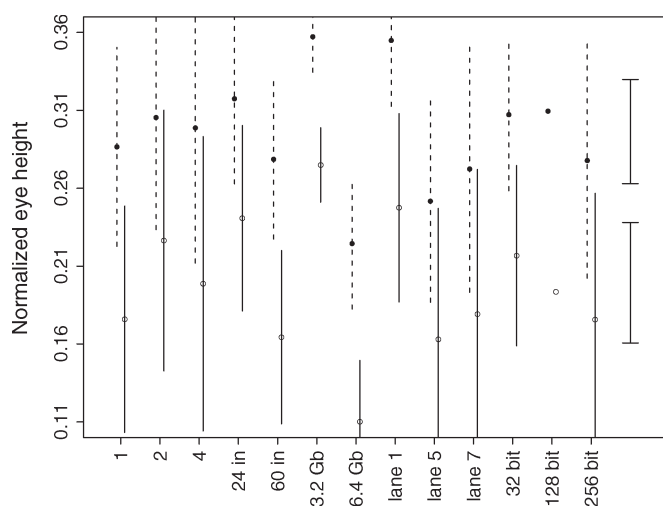


Fig. 9. Plot of difference between mean normalized eye height for printed circuit board with calibration (solid circles, dashed error bars) and mean normalized eye height without calibration (empty circles, solid error bars). Error bars are 95% confidence intervals of each factor while the right-most column shows 95% confidence intervals pooled over all factors.

too meaningful, and a more extensive study is needed to make conclusions regarding individual factors.

V. CONCLUSION

Software for de-embedding measurement mismatch, loss, and sampler response from eye diagram measurements is available for real-time and equivalent-time oscilloscopes from most manufacturers. The accuracy of the de-embedded results depends on the noise and timing accuracy of the measurements, the accuracy of the system response employed for deconvolution, and the manner in which the deconvolution noise amplification is controlled (regularized). In commercial systems, the regularization framework varies from platform to platform. In some cases, the regularization parameter (or its equivalent) can be arbitrarily adjusted by the user. These variations can have a significant effect on the de-embedded waveform. As an example, changes in a de-embedded waveform can clearly be observed while manually adjusting the cutoff frequency used for de-embedding about one meter of cable. Without a well-defined regularization framework (e.g., Tikhonov, truncation,

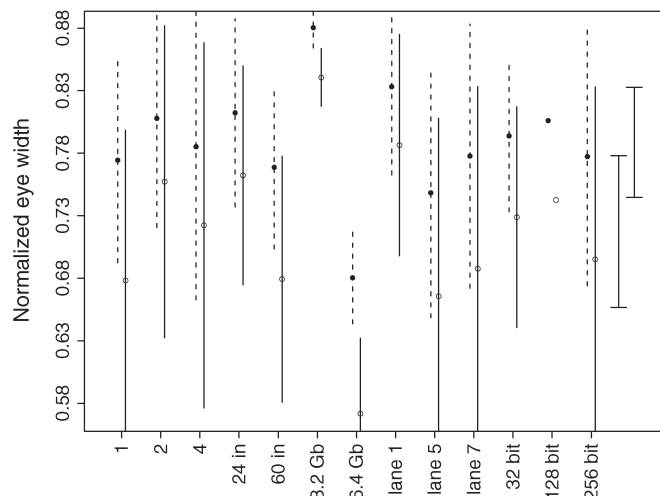


Fig. 10. Plot of difference between mean normalized eye width for printed circuit board with calibration (solid circles, dashed error bars) and mean normalized eye width without calibration (empty circles, solid error bars). Error bars are 95% confidence intervals of each factor while the rightmost column shows 95% confidence intervals pooled over all factors.

etc.) and a regularization parameter selector (or its equivalent), it is unlikely that de-embedded measurements will be repeatable between measurement platforms, regardless of the quality of the system response data.

In this paper, we proposed the Tikhonov regularization strategy with the L-curve regularization parameter selector and used these procedures to de-embed digital waveform measurement distortions caused by cable loss, mismatch, and sampler response. We applied traceable measurements to construct a system response function over a broad range of loss, mismatch, and oscilloscope response functions and de-embedded their effect from the measurements. We found that our previous L-curve selector ([5], [16]) needed to be modified to accommodate multiple curvature maxima. Use of the largest λ corresponding to a maximum gave consistent results. We also found that in some cases with high bandwidth and low noise, the curvature maximum was very weak. In these cases, a minimum bound for λ may be useful, as suggested in [11].

We have noticed it commonly said, after visual inspection, that the de-embedded waveform appears “improved,” implying that it is more *accurate*. We maintain that improvement of any observable waveform parameter (e.g., eye height, transition duration, eye width) is not necessary for an accurate result. For example, the transition duration of a digital waveform can be made almost arbitrarily small by application of the wrong system response function. We have also seen examples where a more closed eye is the more correct result. Accuracy can only be validated by a careful uncertainty analysis of the deconvolution algorithms and the estimated system response.

We used a statistical analysis of eye height and width to demonstrate that 1) distortions due to the measurement system were significant (even in the case where no cables were included) and 2) the corrections of the various measurements were consistent in the generator/oscilloscope configurations considered in this work. De-embedding resulted in an increase in eye height that was significant at the 95% confidence level. In the experiment with losses added by cables only, we showed

significantly increased eye width. In the measurement of the eye of the signal transmitted through the printed circuit boards, we observed noticeable, but not significant, increase in the eye width. Because our results are consistent for various system response functions, we are confident that our numerical algorithms are behaving as designed. All the measurements that we used to construct our system response function were traceable to fundamental physical principles ([17], [21]–[27]), thus we are confident that our de-embedded waveforms are accurate.

As next steps, the robustness of the L-curve, and other λ selectors, with respect to varying noise levels should be investigated. Also, the uncertainties in our system response function should be propagated through to the de-embedded waveform to quantify the accuracy of our waveforms. These system response uncertainties are correlated, and the correlations must be accounted for to accurately estimate the time and magnitude of the expected clumps of uncertainty. However, the covariance matrix-based methods used in [16], [24], and [25] become impractical when the number N of elements of the waveform vector becomes large, because the covariance matrix scales as N^2 . We are working on methods to reduce the amount of data required to adequately account for possible long-time correlations arising in our waveform measurements. The scaled Jacobian method of [32] is one possible approach. Finally, the extent to which our digital signal measurements are effected by sampler nonlinearity and source impedance nonlinearity should be investigated.

APPENDIX A SYSTEM RESPONSE FUNCTION

A. Microwave Circuit Theory Preliminaries and Direct Connection Between a Signal Generator and the Oscilloscope

We start with an abbreviated version of the background provided in [24]. The complex power-normalized (frequency-domain) forward and backward wave amplitudes³ a and b normalized to a $50\ \Omega$ reference impedance are commonly used in place of voltages and currents at microwave frequencies [33].

When the system is time invariant and linear, the circuit diagram in Fig. 11 can be applied (see [24] for details). The generator can be described by its forward-wave source amplitude b_g and its reflection coefficient Γ_g . Conversions between the wave-based representation and the Thevenin and Norton equivalent circuits can be found in [21], [34], and [35]. The oscilloscope on the right-hand side of Fig. 11 can be characterized by its reflection coefficient Γ_s and its frequency response function i.e., the Fourier transform \hat{h}_0 of its impulse response $h_0(t)$. Generally, \hat{h}_0 is designed to behave as a low-pass filter.

For quasi-TEM guides with a suitable choice of voltage path, we can express the complex voltage amplitude \hat{v}_g of the “forward voltage wave” associated with the wave amplitude b_g in Fig. 11 as [24], [33]

$$\hat{v}_g = b_g \sqrt{50\ \Omega}. \quad (6)$$

³As there is no risk of confusing time- and frequency-domain representations of the a and b waves, power, and scattering parameters, we neglect the hats on these quantities to simplify our presentation.

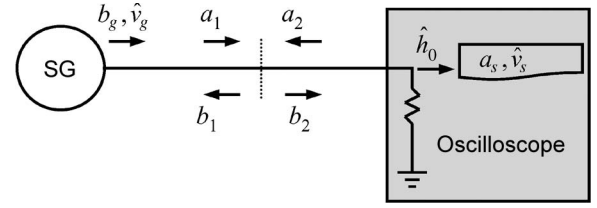


Fig. 11. Schematic diagram showing a signal generator connected directly to an oscilloscope and the quantities of interest (defined in text). The junction between the devices is represented as a dotted line.

The square root of $50\ \Omega$ converts the power-normalized wave amplitude b_g to a voltage. The voltage \hat{v}_g is the voltage amplitude that the generator would produce across a perfect $50\ \Omega$ load. The relation between the voltage \hat{v}_s that the oscilloscope measures (on its display or in a stored data file) and the wave $a_s = \hat{h}_0 b_2$ is

$$\hat{v}_s = a_s \sqrt{50\ \Omega}. \quad (7)$$

The voltage \hat{v}_g should not be confused with the total voltage at the generator’s output port when the impedance of the oscilloscope is not equal to $50\ \Omega$. This is because the voltage at the output of the source depends on the impedance of the load connected to it. Measurement accuracy can be improved, particularly at high frequencies, by accounting for the imperfect impedances of the generator, oscilloscope, and device under test with a “mismatch correction.”

Now, we can relate the generated signal to the voltage measured by the oscilloscope. The wave amplitudes at junction between the generator and the oscilloscope are given by [34]

$$a_1 = b_g + \Gamma_g b_1 \quad (8)$$

$$a_2 = \Gamma_s b_2. \quad (9)$$

Since the generator and oscilloscope are connected directly together, the waves are continuous across the junction, and we have $a_1 = b_2$ and $b_1 = a_2$. Combining equations (6)–(9), we obtain

$$\hat{v}_g = \hat{h}_A^{-1} \hat{v}_s \quad (10)$$

where we define the *system* response function \hat{h}_A when the generator and oscilloscope are directly connected as

$$\hat{h}_A = \hat{h}_0 (1 - \Gamma_s \Gamma_g)^{-1}. \quad (11)$$

Notice that (10) is written in terms of an estimated input function on the left-hand side and, on the right-hand side, an inverse system response function operating on a measurement, and should be compared with the frequency by frequency expansion of the inverse of (3).

B. De-Embedding Measurements That Include One Adapter, Cable, or Other Two-Port Connection

We next show how a device \mathcal{D} connected between the generator and oscilloscope alters the signal and how its effects can be

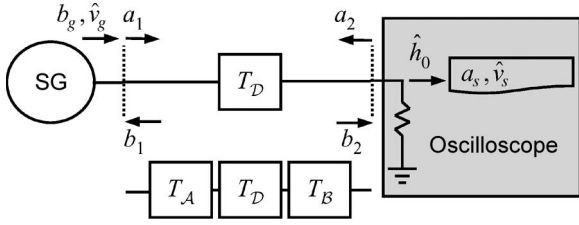


Fig. 12. Schematic diagram showing a signal generator connected to an oscilloscope through a device under test \mathcal{D} . The device is characterized by its scattering matrix or its cascade matrix $\mathbf{T}_{\mathcal{D}}$. The generator and oscilloscope can also be connected to the device through cables/test fixtures \mathcal{A} and \mathcal{B} that are characterized by the cascade matrices $\mathbf{T}_{\mathcal{A}}$ and $\mathbf{T}_{\mathcal{B}}$.

de-embedded. Referring to Fig. 12, we can relate the measured signal to the desired signal by use of the cascade matrix \mathbf{T} , defined as

$$\mathbf{T}_{\mathcal{D}} = \frac{1}{S_{21}} \begin{pmatrix} -\Delta & S_{11} \\ -S_{22} & 1 \end{pmatrix} \quad (12)$$

where

$$\Delta = S_{11}S_{22} - S_{12}S_{21} \quad (13)$$

and S_{ij} are the S-parameters of the device \mathcal{D} . We then relate the waves at the generator port to the waves at the oscilloscope port using the cascade matrix,

$$\begin{pmatrix} b_1 \\ a_1 \end{pmatrix} = \mathbf{T}_{\mathcal{D}} \begin{pmatrix} a_2 \\ b_2 \end{pmatrix}. \quad (14)$$

Using (8) and (9), we obtain

$$\begin{pmatrix} b_1 \\ b_g + \Gamma_g b_1 \end{pmatrix} = \hat{h}_0^{-1} \mathbf{T}_{\mathcal{D}} \begin{pmatrix} \Gamma_s \\ 1 \end{pmatrix} a_s. \quad (15)$$

Finally, using (12) and eliminating b_1 from (15), we obtain

$$\hat{v}_g = \hat{h}_B^{-1} \hat{v}_s \quad (16)$$

where

$$\hat{h}_B = \hat{h}_0 S_{21} (1 - S_{22} \Gamma_s - S_{11} \Gamma_g + \Gamma_s \Gamma_g \Delta)^{-1}. \quad (17)$$

C. Transmission Through a Lossy Device

Here, we want to solve for the effect of a lossy device \mathcal{D} on the transmitted signal when $\Gamma_s = \Gamma_g = 0$. Rewriting (16) and (17), we see that the transmitted wave is given by

$$S_{21} \hat{v}_g = \hat{h}_0^{-1} \hat{v}_s. \quad (18)$$

In a typical measurement, $\Gamma_s, \Gamma_g \neq 0$. However, we still want to solve for the wave that *would* be transmitted through \mathcal{D} if it were connected to an ideal generator and load; that is, we want to solve for $S_{21} \hat{v}_g$. In this case, (18) becomes

$$S_{21} \hat{v}_g = \hat{h}_C^{-1} \hat{v}_s \quad (19)$$

where

$$\hat{h}_C = \hat{h}_0 (1 - S_{22} \Gamma_s - S_{11} \Gamma_g + \Gamma_s \Gamma_g \Delta)^{-1}. \quad (20)$$

The form of (19) warrants some discussion. First, S_{21} is shown explicitly as part of the unknown $S_{21} \hat{v}_g$ but is also

included in the system response function \hat{h}_C . That is, we must measure S_{21} to calibrate our measurement of the signal transmitted through \mathcal{D} . Why do we not measure S_{21} , multiply by a reasonable model for the generator signal, inverse DFT, and be done with the problem? We take the approach that a direct measurement of the waveform does not require any approximations or assumptions regarding the generator waveform and can therefore give a more accurate estimate of the transmitted waveform.

Also, various approximations could be made to reduce the number of multipath terms in (20). However, measurements of the device's S-parameters would typically be required to judge the validity of the approximation, perhaps canceling any benefit from the approximations. We found that in the cases studied here, the multipath term in (20) and in (23) had negligible effect on the measured eye height and width. We caution the reader that these are not general results and that approximations regarding the multipath effects should be attempted only after a careful, contextual study of the measurement system and device under test.

Finally, the signal $S_{21} \hat{v}_g$ transmitted by \mathcal{D} changes when \hat{v}_g is changed, for example, by using a different generator. One might consider calculation of the transmission of a standardized voltage source \hat{V}_S , as a way to obtain consistent measurements with different generators. This might be accomplished by measuring the Fourier transform \hat{v}_g of the generator waveform independently of the transmission measurement. The new standardized waveform is given by $(S_{21} \hat{v}_g)(\hat{V}_S / \hat{v}_g)$, where \hat{V}_S is the Fourier transform of the waveform produced by the standard generator. However, we expect that this naive approach will be unstable in some cases because of zeros in the spectrum of \hat{v}_g . Duty cycle distortion in either the desired or actual generator may further complicate the problem. In this paper, we assume that the source is fixed and approximates an ideal generator. We may, in a later work, consider regularized transformation to calculate the transmitted waveform when different or non-standard generators are utilized.

D. Device Embedded Between Two Test Fixtures

We now refer to the lower part of Fig. 12. Proceeding as in the previous section, we write

$$\begin{pmatrix} b_1 \\ b_g + \Gamma_g b_1 \end{pmatrix} = \hat{h}_0^{-1} \mathbf{T}_{\mathcal{A}} \mathbf{T}'_{\mathcal{D}} \mathbf{T}_{\mathcal{B}} \begin{pmatrix} \Gamma_s \\ 1 \end{pmatrix} a_s \quad (21)$$

where

$$\mathbf{T}'_{\mathcal{D}} = S_{21} \mathbf{T}_{\mathcal{D}}.$$

We make the substitution

$$\begin{pmatrix} P \\ Q \end{pmatrix} = \mathbf{T}_{\mathcal{A}} \mathbf{T}'_{\mathcal{D}} \mathbf{T}_{\mathcal{B}} \begin{pmatrix} \Gamma_s \\ 1 \end{pmatrix}$$

and solve (21) for the response of device \mathcal{D} in a lossless, impedance-matched measurement system:

$$S_{21} \hat{v}_g = \hat{h}_D^{-1} \hat{v}_s \quad (22)$$

where

$$\hat{h}_D = \hat{h}_0(Q - \Gamma_g P)^{-1}. \quad (23)$$

As in the previous section, exact calculation of the transmitted waveform requires inclusion of all four S-parameters in T'_D .

APPENDIX B

CONSTRUCTING AN EYE DIAGRAM FROM A WAVEFORM

The waveform vectors \mathbf{v}_s and \mathbf{v}_g contain one or more 256-bit words and are measured in an 80 ns epoch. We use these waveforms to construct eye diagrams which, in turn, are used to calculate the parameters *eye height*, *jitter*, and *eye width* by the procedures described in [30]. We construct an eye diagram by mapping each bit from the parent waveform into a time interval $(t_0, t_0 + \Psi)$, for $\Psi \geq T$, where T is the bit period. That is, if the waveform is represented by the set of ordered pairs (t_n, v_n) , the eye waveform is represented by the set of ordered pairs (ψ_n, v_n) , where

$$t_n \equiv \psi_n \pmod{\Psi} - \Psi_0 \quad (24)$$

and Ψ_0 is used to center the eye.

There is an implicit assumption that an eye is periodic on average, that is, an eye that spans one bit period is equivalent to an eye that is shifted in time by $\pm T$. For example, if a sampling oscilloscope is used to acquire an eye diagram, and the displayed time interval is greater than $2T$, two eyes will be displayed. We expect that eye parameters extracted from each displayed eye would be indistinguishable. However, when we construct an eye from a sequential waveform that spans only a small number of bits and use $\Psi > T$, the eye does not appear to be periodic. Furthermore, it is impossible to estimate the width of an eye diagram that spans exactly one bit period without assuming that the eye waveform at time ψ is equivalent to the eye waveform at time $\psi \pm T$. Therefore, we must synthesize an eye diagram with duration longer than T while enforcing periodicity and using only the small amount of data we have. We must also choose Ψ_0 to center the eye in this extended eye waveform epoch. For our application, we extend the eye from the original eye with $\psi \in [0, T)$ to $\psi' \in (-T/4, 5T/4)$ and find an acceptable value of Ψ_0 that places the leftmost eye level crossing instant approximately at $\psi' = 0$ by use of the following iterative procedure:

- 1) Do.
- 2) Let $\Psi_0 = -T/4$.
- 3) Map the waveform to an eye diagram $E_0 = \{(\psi_n, v_n)\}$ by use of (24) above with $\Psi = T$.
- 4) Find all ordered pairs in E_0 where $0 \leq \psi_j < T/4$, and create copy of these pairs right shifted by one period: $E_+ = \{(\psi_j + T, v_j)\}$.
- 5) Find all ordered pairs in E_0 where $3T/4 \leq \psi_k < T$, and create copy of these pairs left shifted by one period: $E_- = \{(\psi_k - T, v_k)\}$.
- 6) The extended eye is now the sum of the sets E_0 , E_+ , and E_- .
- 7) Calculate left and right level crossing times t_L and t_R .

$$8) \Psi_0 = \Psi_0 + \delta T.$$

$$9) \text{ Loop until } (-\Delta T < t_L < \Delta T \text{ and } T - \Delta T < t_R < T + \Delta T).$$

We use $\delta T = 0.025T$ and $\Delta T = 0.05T$. In some high jitter cases, it may be advisable to extend the eye diagram to the time interval $\psi' \in (-T/2, 3T/2)$.

REFERENCES

- [1] R. F. Bauer and L. Penfield, "De-embedding and unterminating," *IEEE Trans. Microw. Theory Tech.*, vol. MTT-22, no. 3, pp. 282–288, Mar. 1974.
- [2] *Agilent Signal Integrity Series, Part 3: The ABCs of De-Embedding*, Agilent Technol., Inc. Santa Clara, CA, 2007.
- [3] D. Derickson and M. Muller, Eds., *Digital Communications Test and Measurement*. Upper Saddle River, NJ: Prentice-Hall, 2008.
- [4] R. White, "De-embedding improves measurement accuracy," *Test and Measurement World*, pp. 32–35, Nov. 2010.
- [5] P. D. Hale and A. Dienstfrey, "Waveform metrology and the quantitative study of regularized deconvolution," in *Proc. IEEE I2MTC*, May 3–6, 2010, pp. 386–391.
- [6] P. C. Hansen, *Rank-Deficient and Discrete Ill-Posed Problems: Numerical Aspects of Linear Inversion*, ser. *Monographs on Mathematical Modeling and Computation*. Philadelphia, PA: SIAM, 1998.
- [7] C. R. Vogel, *Computational Methods for Inverse Problems*, ser. *Frontiers in Applied Mathematics*. Philadelphia, PA: SIAM, 2002.
- [8] P. C. Hansen, *Discrete Inverse Problems: Insight and Algorithms*, ser. *Fundamentals of Algorithms*. Philadelphia, PA: SIAM, 2010.
- [9] A. N. Tikhonov and V. Y. Arsenin, *Solutions of Ill-Posed Problems*. Washington, DC: V. H. Winston and Sons, 1977.
- [10] T. Correia, A. Gibson, M. Schweiger, and J. Hebden, "Selection of regularization parameter for optical topography," *J. Biomed. Opt.*, vol. 14, no. 3, pp. 034 044-1–034 044-11, May/Jun. 2009.
- [11] F. Bauer and M. A. Lukas, "Comparing parameter choice methods for regularization of ill-posed problems," *Math. Comput. Simul.*, vol. 81, no. 9, pp. 1795–1841, May 2011.
- [12] S. M. Riad, "The deconvolution problem: An overview," *Proc. IEEE*, vol. 74, no. 1, pp. 82–85, Jan. 1986.
- [13] W. L. Gans, "Calibration and error analysis of a picosecond pulse waveform measurement system at NBS," *Proc. IEEE*, vol. 74, no. 1, pp. 86–90, Jan. 1986.
- [14] T. Daboczi, "Nonparametric identification assuming two noise sources: A deconvolution approach," *IEEE Trans. Instrum. Meas.*, vol. 47, no. 4, pp. 828–832, Aug. 1998.
- [15] H. W. Engl, M. Hanke, and A. Neubauer, *Regularization of Inverse Problems*. Norwell, MA: Kluwer, 2000.
- [16] P. D. Hale, A. Dienstfrey, J. C. M. Wang, D. F. Williams, A. Lewandowski, D. A. Keenan, and T. Clement, "Traceable waveform calibration with a covariance-based uncertainty analysis," *IEEE Trans. Instrum. Meas.*, vol. 58, no. 10, pp. 3554–3568, Oct. 2009.
- [17] P. D. Hale, C. M. Wang, D. F. Williams, K. A. Remley, and J. Wepman, "Compensation of random and systematic timing errors in sampling oscilloscopes," *IEEE Trans. Instrum. Meas.*, vol. 55, no. 6, pp. 2146–2154, Dec. 2006.
- [18] Timebase Correction Software. [Online]. Available: http://www.nist.gov/pml/optoelectronics/sources_detectors/tbc.cfm
- [19] P. T. Boggs, R. H. Byrd, and R. B. Schnabel, "A stable and efficient algorithm for nonlinear orthogonal distance regression," *SIAM J. Sci. Stat. Comput.*, vol. 8, no. 6, pp. 1052–1078, Nov. 1987.
- [20] T. S. Clement, P. D. Hale, D. F. Williams, C. M. Wang, A. Dienstfrey, and D. A. Keenan, "Calibration of sampling oscilloscopes with high-speed photodiodes," *IEEE Trans. Microw. Theory Tech.*, vol. 54, no. 8, pp. 3173–3181, Aug. 2006.
- [21] D. F. Williams, P. D. Hale, T. S. Clement, and J. M. Morgan, "Mismatch corrections for electro-optic sampling systems," in *Proc. 56th ARFTG Conf. Digest*, Dec. 2000, pp. 141–145.
- [22] D. F. Williams, P. D. Hale, T. S. Clement, and J. M. Morgan, "Calibrating electro-optic sampling systems," in *IMS Conf. Dig.*, May 2001, vol. 1473, pp. 1527–1530.
- [23] T. S. Clement, D. F. Williams, P. D. Hale, and J. M. Morgan, "Calibrated photoreceiver response to 110 GHz," in *Proc. Conf. Digest 15th Annu. Meeting IEEE Lasers Electro-Opt. Soc.*, Glasgow, U.K., Nov. 10–14, 2002, pp. 877–878.
- [24] D. F. Williams, T. S. Clement, P. D. Hale, and A. Dienstfrey, "Terminology for high-speed sampling-oscilloscope calibration," in *Proc. 68th ARFTG Microw. Meas. Conf. Digest*, Boulder, CO, Nov. 30–Dec. 1, 2006.

- [25] D. F. Williams, A. Lewandowski, T. S. Clement, C. M. Wang, P. D. Hale, J. M. Morgan, D. A. Keenan, and A. Dienstfrey, "Covariance-based uncertainty analysis of the NIST electrooptic sampling system," *IEEE Trans. Microw. Theory Tech.*, vol. 54, no. 1, pp. 481–491, Jan. 2006.
- [26] A. Dienstfrey, P. D. Hale, D. A. Keenan, T. S. Clement, and D. F. Williams, "Minimum-phase calibration of sampling oscilloscopes," *IEEE Trans. Microwave Theory Tech.*, vol. 54, no. 8, pp. 3197–3208, Aug. 2006.
- [27] D. F. Williams, C. M. Wang, and U. Arz, "An optimal vector-network-analyzer calibration algorithm," *IEEE Trans. Microw. Theory Tech.*, vol. 51, no. 12, pp. 2391–2401, Dec. 2003.
- [28] S. Ramo, J. R. Whinnery, and T. Van Duzer, *Fields and Waves in Communications Electronics*. Hoboken, NJ: Wiley, 1994.
- [29] F. S. V. Bazan and J. B. Francisco, "An improved fixed-point algorithm for determining a Tikhonov regularization parameter," *Inverse Probl.*, vol. 25, no. 4, p. 045007, Apr. 2009.
- [30] J. Jargon, C. M. Wang, and P. D. Hale, "A robust algorithm for eye-diagram analysis," *J. Lightw. Technol.*, vol. 26, no. 21, pp. 3592–3600, Nov. 1, 2008.
- [31] G. E. P. Box, W. G. Hunter, and J. S. Hunter, *Statistics for Experimenters*. New York: Wiley, 1978.
- [32] A. Lewandowski, D. F. Williams, P. D. Hale, C. M. Wang, and A. Dienstfrey, "Covariance-matrix vector-network-analyzer uncertainty analysis for time- and frequency-domain measurements," *IEEE Trans. Microw. Theory Tech.*, vol. 58, no. 7, pp. 1877–1886, Jul. 2010.
- [33] R. B. Marks and D. F. Williams, "A general waveguide circuit theory," *J. Res. Nat. Inst. Std. Technol.*, vol. 97, no. 5, pp. 533–562, Oct. 1992.
- [34] D. M. Kerns and R. W. Beatty, *Basic Theory of Waveguide Junctions and Introductory Microwave Network Analysis*, 1st ed. Oxford, NY: Pergamon, 1967.
- [35] P. D. Hale, T. S. Clement, D. F. Williams, E. Balta, and N. D. Taneja, "Measurement of chip photodiode response for gigabit applications," *J. Lightw. Technol.*, vol. 19, no. 9, pp. 1333–1339, Sep. 2001.



C. M. Jack Wang received the Ph.D. degree in statistics from Colorado State University, Fort Collins, in 1978.

He joined the Statistical Engineering Division, National Institute of Standards and Technology, Boulder, CO, in 1988. He has published over 70 journal articles. His research interests include statistical metrology and the application of statistical methods to physical sciences.

Dr. Wang is a Fellow of the American Statistical Association (ASA). He is the recipient of the Department of Commerce Bronze Medals and several awards from ASA.



Brett Grossman is a Senior Staff Engineer and currently leads the signal integrity pathfinding efforts for Intel's Sort Test Technology Development organization. He is responsible for identifying and developing high frequency signal delivery technologies for interfaces that are > 5 years from production. His current efforts focus on the development of characterization and modeling tools for passive 12-port interconnects in PCB's, ceramics, and connectors to beyond 60 GHz. Prior to joining Sort Test Technology Development, he spent 11 years working for Intel's Test Operations organization. While in this role, he developed hardware for interfaces up to 40 Gb/s, and power delivery solutions for up to 200 W devices in the production test environment. He was also responsible for developing many of the electrical characterization, analysis, and modeling techniques that continue to be utilized by these teams. In 2005, he was appointed a Sr. Signal Integrity Technologist for Intel Corporation, Hillsboro, OR. He has published over a dozen papers.

Mr. Grossman has been an IEEE member for 18 years and is involved in the EMC, CPMT, and MTT societies. He is currently an officer in the Portland chapter of the IEEE MTT/ED societies. He has served on the technical program committee for the IEC DesignCon conference, the IEEE International EMC Symposium, ARFTG, and Intel's Design and Test Technology Conference. He is also a Cofounder and program committee member for the Intel High Frequency Measurement Workshop. He has received a Best Poster Paper award from the ARFTG conference, as well as Best Technical Presentation and Best Tutorial awards from the IEEE Semiconductor Wafer Test Workshop.



Mathew Claudius received the B.S. degree in computer engineering from Vanderbilt University, Nashville, TN, in 2000.

He joined Intel Corporation, Santa Clara CA, in 2000 and is currently an Electrical Analysis Engineer in Intel's Sort Test Technology Department. Over the last 11 years, he has worked in probecard design, model building, and signal integrity simulations, and designed new techniques for establishing model validity through correlation to measured data. Currently, his focus is on metrology development for

time domain high-speed IO measurements of test interface boards to facilitate long-range test planning.



José L. Torres received the Ph.D. degree in electrical engineering from the University of Houston, Houston, TX, in 2001. His Ph.D. research was involved in semiconductor processing and methods for next generation lithography.

From 2002 to 2004, he worked as Research Assistant Professor in the Department of Electrical Engineering, the University of Houston, conducting research in next generation lithography for semiconductor processing. He joined Intel Corporation, Chandler, AZ, in 2004 as a Test Engineer, where

he develops HVM test tooling solutions for high speed IOs of chipsets and processors. He is the author of 15 published technical papers and holds one patent in the area of semiconductor processing.



Paul D. Hale (M'01–SM'01) received the Ph.D. degree in applied physics from the Colorado School of Mines, Golden, in 1989.

He has been with the Optoelectronics Division, National Institute of Standards and Technology (NIST), Boulder, CO since 1989, where he conducts research on broadband optoelectronic device and signal metrology. He has been Leader of the High-Speed Measurements Project in the Sources and Detectors Group since 1996. His current technical work focuses on extending both time- and frequency-domain optoelectronic measurements to beyond 110 GHz, implementing a novel covariance-based uncertainty analysis that can be used for both time- and frequency-domain quantities, and disseminating NIST traceability through high-speed electronic and optoelectronic measurement services.

Dr. Hale was an Associate Editor of Optoelectronics/Integrated optics for the IEEE JOURNAL OF LIGHTWAVE TECHNOLOGY from June 2001 to March 2007. He is the recipient of the Department of Commerce Bronze, Silver, and Gold awards, the Allen V. Astin Measurement Science Award, two ARFTG Best Paper Awards, and the NIST Electrical Engineering Laboratory's Outstanding Paper Award.



Jeffrey Jargon (M'98–SM'01) received the B.S., M.S., and Ph.D. degrees in electrical engineering from the University of Colorado at Boulder, Boulder, in 1990, 1996, and 2003, respectively.

He has been a Staff Member of the National Institute of Standards and Technology, Boulder, CO, since 1990 and has conducted research in the areas of vector network analyzer calibrations, microwave metrology, and optical performance monitoring. He is presently a member of the High-Speed Measurements Project in the Optoelectronics Division. He

has published over 70 technical articles.

Dr. Jargon is an ASQ Certified Quality Engineer, and a registered Professional Engineer in the State of Colorado. He has received four best paper awards, an URSI Young Scientist Award, and a Department of Commerce Silver Medal Award.



Andrew Dienstfrey received the B.A. degree in mathematics from Harvard College, Cambridge, MA, in 1990 and the Ph.D. degree in mathematics from the Courant Institute of Mathematical Sciences, New York, NY in 1998.

From 1998 to 2000, he was a Post-Doctoral Scientist at the Courant Institute investigating methods for remote sensing of dielectric properties of superconducting thin films. He joined the Mathematical and Computational Sciences Division, National Institute of Standards and Technology, Boulder, CO, in 2000.

In 2008, he initiated the Information Technology Laboratory's Program in Virtual Measurement Systems for which he presently serves as Program Manager. His research interests include uncertainty quantification for scientific computation, theoretical and computational aspects of periodic scattering problems in acoustics and electromagnetics, and linear systems analysis.



Dylan F. Williams (M'80–SM'90–F'02) received the Ph.D. degree in electrical engineering from the University of California, Berkeley, in 1986.

He joined the Electromagnetic Fields Division, National Institute of Standards and Technology, Boulder, CO, in 1989 where he develops electrical waveform and microwave metrology. He has published over 80 technical papers.

Dr. Williams served as Editor of the IEEE TRANSACTIONS ON MICROWAVE THEORY AND TECHNIQUES from 2006 to 2010. He is the recipient of the Department of Commerce Bronze and Silver Medals, the Astin Measurement Science Award, two Electrical Engineering Laboratory's Outstanding Paper Awards, three Automatic RF Techniques Group Best Paper Awards, the ARFTG Automated Measurements Technology Award, and the IEEE Morris E. Leeds Award.